Advanced Materials Technologies

ADVANCED MATERIALS TECHNOLOGIES
www.advmattechnol.com

RESEARCH ARTICLE

A High-Sensitivity Wearable Sensor for Precision Recognition of Human Arm Joint Movements Using CNN

Junlei Wang[1] | Tianyang Geng[1,2] | Xilong Kang[1] | Guobiao Hu[2]

[1]School of Mechanical and Power Engineering, Zhengzhou University, Zhengzhou, China | [2]Thrust of the Internet of Things, The Hong Kong University of Science and Technology (Guangzhou), Guangzhou, China

Correspondence: Xilong Kang (xlkang@zzu.edu.cn) | Guobiao Hu (guobiaohu@hkust-gz.edu.cn)

Received: 26 September 2025 | **Revised:** 10 February 2026 | **Accepted:** 11 February 2026

Keywords: convolutional neural network (CNN) | flexible electronics | P(VDF-TrFE) | sandwich-structured composites | wearable piezoelectric sensors

ABSTRACT

With the cross-integration of flexible electronics and artificial intelligence technologies, high-sensitivity wearable sensors have shown great potential in fields such as medical rehabilitation, human-computer interaction, and sports science. To meet the dual requirements of high sensitivity and flexibility for wearable applications, this study proposes a novel sandwich-structured P(VDF-TrFE)/BTO-OH/P(VDF-TrFE) piezoelectric sensor (SP-sensor) using a fused deposition modeling (FDM) process. This structure effectively combines the high piezoelectricity of BTO nanoparticles with the excellent flexibility of the P(VDF-TrFE) polymer, overcoming the limitations of traditional single-layer piezoelectric sensors. Experimental results demonstrate that the piezoelectric response voltage and current of the SP-sensor are enhanced by 51.1% and 546%, respectively, compared with those of single-layer P(VDF-TrFE) films. With improved piezoelectric performance, the SP-sensor achieves approximately 50% higher sensitivity than the traditional designs. It also exhibits quick response and recovery capabilities, with a response time of 8.1 ms and a recovery time of 64 ms. Additionally, it exhibits excellent fatigue resistance, with no noticeable voltage decay observed after 18,000 cycles of testing. An intelligent wrist motion recognition system, integrating a deep learning algorithm (CNN model), was developed based on this SP-sensor, enabling real-time classification of three types of wrist movement patterns with an identification accuracy of 97.85%. This study, through the innovation in material structure and the integration of AI algorithms, paves the way for the application of next-generation wearable devices in human-machine interaction and medical diagnosis.

1 | Introduction

In recent years, the deep convergence of flexible electronics and artificial intelligence (AI) has catalyzed the rapid advancement of next-generation high-sensitivity wearable sensors [1–4]. Such devices facilitate real-time monitoring of physiological signals (e.g., heart rate, blood pressure, and electromyography), biomechanical motions, and environmental parameters, thereby demonstrating broad applicability in medical rehabilitation [5, 6], human-computer interaction [7–9], and sports science [10]. The core innovation of these sensors lies in their seamless integration of flexibility, micron-level precision, and edge intelligence—capabilities unattainable by conventional rigid sensing devices—positioning them as sensory neural interfaces that bridge the physical and digital worlds [11].

Current-generation wearable devices are often constrained by rigid circuit architectures and low-sensitivity sensing components, restricting their functionality to rudimentary applications, such as heart rate monitoring and step counting. With the advancement of flexible materials like polymer materials and hydrogels, sensors have achieved remarkable characteristics, including ultra-thinness, flexibility, and stretchability [12–14]. Organic piezoelectric polymers, such as polyvinylidene

fluoride (PVDF) and its copolymer poly(vinylidene fluoride-trifluoroethylene, P(VDF-TrFE)), have been widely utilized for fabricating wearable flexible sensors due to their flexibility and biocompatibility. However, their relatively low piezoelectric coefficients (d_{33}) limit the massive production of highly sensitive sensors, significantly reducing the potential applications of PVDF-based sensors [15, 16]. Although various techniques—such as melt spinning, solution spinning, and electrospinning [17]—have been explored to enhance the piezoelectric properties of PVDF, current advancements still fall short of meeting the high sensitivity and flexibility required for wearable sensor applications.

Traditional inorganic piezoelectric materials, such as barium titanate ($BaTiO_3$, BTO) and lead zirconate titanate (PZT), exhibit excellent piezoelectric properties. However, the inherent brittleness limits their applicability in wearable devices, especially in dynamic deformation scenarios involving bending and stretching [18, 19]. To leverage the advantages of both organic and inorganic materials, many researchers have been committed to developing PVDF/ceramic composite piezoelectric films. One common approach is blending inorganic piezoelectric materials with PVDF-based polymers via multiphase composite fabrication. A notable example is the work by Chen et al. [20], who successfully incorporated BTO nanoparticles into P(VDF-TrFE) and synthesized a micro-pillar array of the nanocomposite. The sensor fabricated from this high-performance composite material demonstrated remarkable electrical outputs, with a maximum piezoelectric response voltage of 13.2 V, a current of 0.33 μA, and an impressive sensitivity of 257.9 mV/N. However, this method cannot avoid issues such as the degradation of piezoelectric and mechanical properties caused by the aggregation of high-content ceramic particles in the polymer matrix. As a result, some researchers have started exploring other advanced preparation processes. For example, Ye et al. [21] prepared P(VDF-TrFE)/boron nitride nanotubes (BNNTs) nanocomposite micropillar arrays with enhanced performance and excellent neutron radiation shielding by a reliable nanoimprint lithography. The composite material exhibits excellent piezoelectric properties, with a voltage output reaching up to 22 V and a sensitivity of 275 mV/N. However, the relatively complex preparation process and strict conditions for the nanowires severely limit their large-scale industrial production. Therefore, there is a need to develop wearable flexible sensors that feature both facile processing and excellent performance.

In this context, wearable sensors featuring sandwich structures have emerged. These sensors exhibit excellent mechanical properties and piezoelectric performance due to the combination of the flexibility of polymer materials and the high-voltage properties of piezoelectric ceramics [22, 23]. Le et al. [24] reported a sandwich-structured composite piezoelectric material, constructed by depositing polydopamine (PDA)-modified $BaTiO_3$ nanoparticles on both sides of a P (VDF-TrFE) film via a two-step adsorption-annealing method. The piezoelectric coefficient of this composite material is 14.6 pC/N, the output voltage reaches up to 6 V, and the pressure sensitivity is 288 mV/N. Peng et al. [25] reported a composite material with a sandwich structure constructed by embedding a single-crystal BTO thin film, prepared by etching a water-soluble sacrificial layer, between two layers of PVDF-TrFE films. This composite exhibited improved ferroelectric and piezoelectric properties. However, most existing studies have only demonstrated that the sandwich structure can generate distinct piezoelectric signals in response to different motion patterns, demonstrating their potential as wearable human-body sensors.

Notably, the advent of AI algorithms has further enhanced the performance of these sensors [26, 27]. Deep learning models have achieved real-time analysis of complex signals, such as abnormal electrocardiograms and gait imbalances, by training on massive physiological datasets [28, 29]. Gu et al. [30] developed a human gait recognition system that integrates a flexible piezoelectric sensor array and a convolutional neural network (CNN), achieving a recognition rate of up to 94.7% for various human gaits. Sun et al. [31] developed an ultra-thin flexible sensor capable of detecting subtle skin deformation induced by human pulses. When integrated with a 2D CNN model, this sensor achieved an identification accuracy of 93.75% for common cardiovascular diseases.

This study proposes a sandwich-structured composite material based on hydroxyl-modified barium titanate nanoparticles (BTO-OH). Via a melt deposition process, the BTO-OH layer is embedded between two layers of P (VDF-TrFE) films to form a flexible piezoelectric composite system with the structure P (VDF-TrFE)/BTO-OH/P (VDF-TrFE). The experimental results show that this structure increases the β-phase crystallinity of the composite material to 93.6%. Through synergistic effects of the piezoelectric properties and the interface, the output voltage, current, and pressure sensitivity are significantly enhanced. Furthermore, the sandwich-structured piezoelectric sensor (SP-sensor) prepared can produce a voltage of 15 V, a current of 0.97 μA under an external force of 20 N. It exhibits a voltage sensitivity of 396 mV/N and a current sensitivity of 33.6 nA/N, with excellent durability, as the output remains stable after 18,000 cycles. When integrated with a convolutional neural network (CNN) model, the device can accurately recognize human wrist movements with a recognition accuracy rate of 97.85%. This provides a new material solution and technical path for the intelligent applications of wearable devices in fields such as sports posture correction and health monitoring. By synergistically optimizing nanoparticle surface modification and structural design, this study overcomes the traditional trade-off between the high piezoelectric response and flexibility, offering new insights for the development of high-performance wearable flexible sensor devices.

2 | Experiments and Methods

Inorganic fillers modified with hydroxyl groups (—OH) have been proven to effectively enhance the interfacial bonding force between two phases and promote the transformation of the polymer's polar crystalline phase due to their ability to form hydrogen bonds with polymer chain segments [32, 33]. Inspired by this, this study proposes a sandwich-structured composite material based on hydroxyl-modified barium titanate nanoparticles (BTO-OH). Using a melt deposition process, the BTO-OH nanoparticle layer is embedded between two layers of P(VDF-TrFE) films to construct a P(VDF-TrFE)/BTO-OH/P(VDF-TrFE) flexible piezoelectric composite. This innovative design is expected to improve

the piezoelectric performance by maximizing the interfacial interactions and crystalline phase transformation.

2.1 | Preparation of BTO-OH

The hydroxyl (—OH) modification of barium titanate ($BaTiO_3$, BTO) nanoparticles (with an average particle size of 50 nm and a specific surface area of 25 m^2/g) was performed using the chemical oxidation method. The process involved adding 1.5 g of BTO nanoparticles into 30 mL of a 30% hydrogen peroxide (H_2O_2) solution. The mixed solution was then transferred to a magnetic stirrer and continuously stirred at room temperature (25 ± 2°C) for 24 h. The strong oxidizing property of H_2O_2 was used to introduce hydroxyl functional groups onto the surface of the BTO nanoparticles. Afterward, the BTO-OH nanoparticles were washed and placed in a vacuum drying oven to be dried at 60°C for 12 h. The resulting surface-hydroxylated BTO nanoparticles were then used to prepare composite materials.

2.2 | Preparation of Sandwich-Structured P(VDF-TrFE)/BTO-OH/P(VDF-TrFE)

In this study, the melt deposition process is used to prepare the flexible piezoelectric film with a P(VDF-TrFE)/BTO-OH/P(VDF-TrFE) sandwich structure. The detailed preparation process is as follows:

2.0 g of poly(vinylidene fluoride-trifluoroethylene) (P(VDF-TrFE)) powder, with a number-average molecular weight of 180,000 Da, was added to 20 mL of N, N-dimethylformamide (DMF, analytical grade, boiling point 153°C) solvent. The mixture was then subjected to magnetic stirring at room temperature (25 ± 2°C) for 6 h at a rotation speed of 500 rpm, allowing the P(VDF-TrFE) to dissolve completely and form a uniform, transparent solution. Subsequently, the solution was poured onto a clean glass plate substrate and placed in a 10 cm×10 cm silicone mold. The substrate was calibrated using a spirit level to ensure horizontal alignment. The substrate was then placed in a vacuum drying oven at 90°C for 12 h to allow sufficient volatilization of the DMF solvent. Once the solvent was completely removed, the film was transferred to a vacuum drying oven and annealed at 120°C for 2 h to eliminate any internal residual stress. Finally, a pure P(VDF-TrFE) film with a thickness of approximately 100 μm was obtained.

1.5 g of hydroxyl-modified barium titanate nanoparticles (BTO-OH) were dispersed in 30 mL of deionized water. The mixture was stirred continuously using a magnetic stirrer at 300 rpm for 30 min to form a stable suspension. The suspension was then evenly dropped onto the surface of the previously prepared P(VDF-TrFE) film. The coated sample was placed in a vacuum drying oven at 50°C for 12 h to remove water and fix the nanoparticles, forming a BTO-OH nanoparticle layer. Following this, the sample was heated on a hot plate at 180°C for 2 h to promote interfacial fusion between the nanoparticles and polymer matrix, resulting in a P(VDF-TrFE)/BTO-OH double-layered structure.

Another pure P(VDF-TrFE) film prepared in the same batch was covered on top of the BTO-OH nanoparticle layer to ensure complete adhesion. The composite structure was then heated in a vacuum drying oven at 180°C for 2 h. Via the thermal melting process, a strong bond between the three layers was achieved. After cooling back to room temperature, the glass plate substrate was peeled off, resulting in a flexible piezoelectric film with a P(VDF-TrFE)/BTO-OH/P(VDF-TrFE) sandwich structure. The total thickness of the film was approximately 200 μm.

2.3 | Preparation of Sandwich-Structured P(VDF-TrFE)

To eliminate the influence of thickness variations on the performance comparison and to ensure that the observed performance enhancement arises solely from structural design innovation, the thickness of the pure P(VDF-TrFE) sensor was strictly controlled to be approximately 200 μm, matching the total thickness of the composite material. The specific preparation procedure is described as follows.

4.0 g of poly(vinylidene fluoride-trifluoroethylene) (P(VDF-TrFE)) powder, with a number-average molecular weight of 180,000 Da, was dissolved into 20 mL of N, N-dimethylformamide (DMF, analytical grade, boiling point 153°C) solvent. The mixture was then subjected to magnetic stirring at room temperature (25 ± 2°C) for 6 h at a rotation speed of 500 rpm, until the P(VDF-TrFE) completely dissolved and formed a homogeneous, transparent solution. Subsequently, the solution was poured onto a clean glass plate substrate, placed in a 10 cm × 10 cm silicone mold. The substrate was calibrated using a spirit level to ensure horizontal alignment. The substrate was then placed in a vacuum drying oven at 90°C for 12 h to fully evaporate the DMF solvent, followed by annealing at 120°C for 2 h to relieve residual internal stresses. Finally, a pure P(VDF-TrFE) film with a thickness of about 200 μm was obtained.

2.4 | Preparation of SP-Sensor

Two copper foil electrodes of identical dimensions were adhered to both sides of the fabricated sandwich-structured composite film. Wires were then connected to the extended copper terminals to establish signal transmission pathways. Therefore, a piezoelectric sensor based on the sandwich-structured composite film was successfully developed. The SP-sensor was then encapsulated with Polyimide (PI) tape to ensure mechanical durability under cyclic stress loading and provide effective environmental shielding against moisture and chemical corrosion.

2.5 | Characterization and Measurement

The cross-sectional morphology of the composites was examined using scanning electron microscopy (SEM) on a Sigma 300. X-ray diffraction (XRD) patterns for all samples were obtained using a Bruker D8 Advance diffractometer. Fourier-transform infrared (FTIR) spectra for chemical characterization were acquired using a micro-infrared spectroscopy instrument (IRTracer100). The electrical characteristics of the composites were measured by using a Keithley 6514 electrometer.

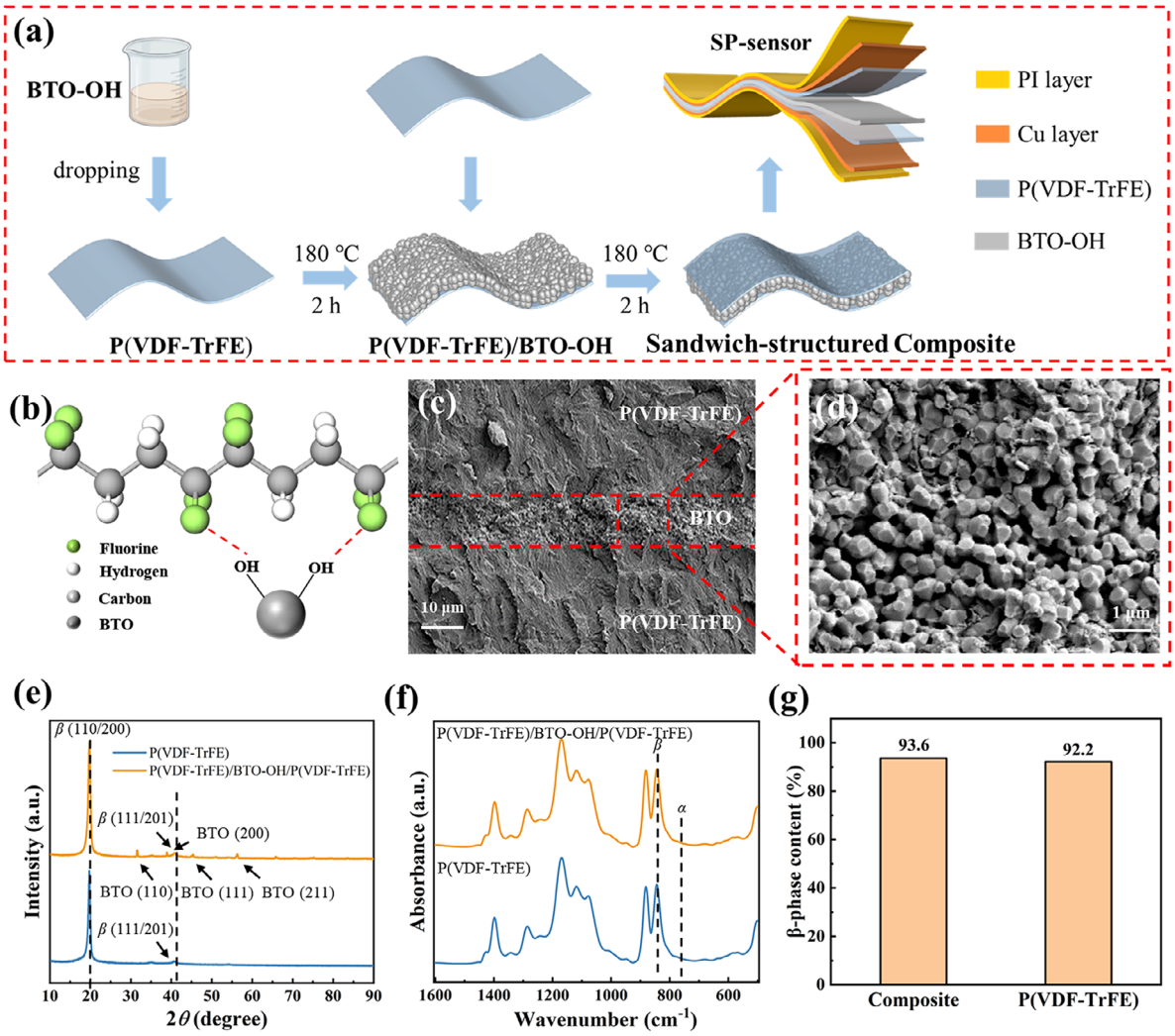

FIGURE 1 | Preparation and Characterization of the SP-sensor. (a) Preparation process of the sandwich structure. (b) Schematic of the molecular structures of BTO and P(VDF-TrFE), and the bonding between the —OH groups attached to BTO molecules and P(VDF-TrFE). (c) and (d) SEM images of the sandwich structure. (e) XRD patterns of the composite films. (f) FTIR spectra of the composite films. (g) β-phase content of the composite and the pure P(VDF-TrFE).

3 | Results and Discussion

3.1 | SP-Sensor Development

The fabrication of sensors with sandwich structures, using polymer materials and piezoelectric ceramics, effectively combines flexibility and high piezoelectricity. As a result, a flexible and high-sensitivity SP-sensor was developed. The synthesis schematic diagram of the flexible composite material with a sandwich structure is shown in Figure 1a. In this study, the BTO-OH nanoparticles were modified with hydroxyl groups (—OH), and the composite material with a sandwich structure was then prepared using the melt deposition method. When the BTO-OH nanoparticle layer was uniformly deposited on top of the P(VDF-TrFE) film, the —OH groups on the BTO nanoparticles interacted with the fluorine groups (—F) on the P(VDF-TrFE) polymer, forming hydrogen bonds. This interaction led to a preliminary combination of the two materials, as shown in Figure 1b. This binding force prevented the BTO-OH nanoparticles from easily detaching from the P(VDF-TrFE) film, laying the foundation for a more stable and secure bond in subsequent steps. Meanwhile, the deposition area of the intermediate layer was controlled within 100 mm × 100 mm to guarantee the uniformity of its thickness. Subsequently, the preliminarily prepared composite material was heated to 180°C and treated for 2 h. The BTO-OH material remained unaffected at this temperature, while the P(VDF-TrFE) material reached its melting point. In this semi-molten state, the P(VDF-TrFE) film allowed the BTO-OH nanoparticles to be embedded within it. After cooling down, a composite material with a strong bond between the BTO-OH and P(VDF-TrFE) layers was formed. By repeating this process on the other side of the P(VDF-TrFE) film, a sandwich-structured composite material was obtained.

The cross-sectional morphology of the composite film with a sandwich structure was captured using SEM, as shown in Figure 1c. The sandwich structure is clearly visible, with the upper and lower layers consisting of P(VDF-TrFE) films, and the middle containing a BTO-OH nanoparticle layer uniformly dispersed throughout. The stacked structure of the BTO-OH

nanoparticle layer can be clearly observed in Figure 1d. The thickness of the P(VDF-TrFE) film is about 100 μm. The BTO-OH nanoparticles are approximately evenly distributed in the P(VDF-TrFE) film and are regularly arranged. Thanks to the thorough melt deposition and the presence of hydroxyl groups, the bonding between BTO-OH and P(VDF-TrFE) is strong, with no observable pores. The XRD patterns of P(VDF-TrFE) and P(VDF-TrFE)/BTO-OH/P(VDF-TrFE), shown in Figure 1e, reveal their crystallization characteristics. In both samples, two distinct diffraction peaks corresponding to the β-phase of P(VDF-TrFE), namely (110/200) and (111/201), were observed at $2\theta = 19.7°$ and 40.8°, with no unique diffraction peaks associated with the α phase. This indicates that the main crystalline component of both composite materials is the β-phase. This is attributed to the annealing treatment applied during the manufacturing process, which promotes the transformation of the non-polar α-phase of the P(VDF-TrFE) into the polar β-phase [34, 35]. However, a notable difference in the peak values of the diffraction peaks of the β-phase was observed between the two samples. The peak value of the XRD pattern represents the crystallinity of the material in a specific crystalline phase, indicating that the addition of the BTO-OH nanoparticle layer has enhanced the β-phase crystallinity of the P(VDF-TrFE) material. Further evidence of the dominance of the β-phase is provided in the Fourier transform infrared spectroscopy (FTIR) results shown in Figure 1f. Both samples exhibit distinct β-phase peaks at 844, 1286, and 1431 cm^{-1}, while weaker α-phase peaks are observed at 763 and 976 cm^{-1} [36, 37]. According to Gregorio's assumption that infrared absorption follows the Lambert-Beer law [38], the relative content of the β-phase in a sample containing both α-phase and β-phase can be expressed as:

$$F(\beta) = \frac{A_\beta}{\left(K_\beta / K_\alpha\right) A_\alpha + A_\beta} \tag{1}$$

where K_α and K_β represent the absorption coefficients of the α-phase and the β-phase, respectively. The value of K_α is 6.1 $\times$ 10^4 cm^2mol^{-1}, and the value of K_β is 7.7 $\times$ 10^4 cm^2mol^{-1}. A_α and A_β are the absorption intensities of the characteristic peaks of the α-phase at 763 cm^{-1} and the β-phase at 844 cm^{-1}, respectively. Using the FTIR results and Equation (1), we calculated that the relative contents of the β-phase in the P(VDF-TrFE) and P(VDF-TrFE)/BTO-OH/P(VDF-TrFE) materials are 92.2% and 93.6%, respectively, as shown in Figure 1g. This slight increase of the β-phase content is likely due to the polarization effect of the BTO-OH nanoparticle layer on top of the P(VDF-TrFE), as well as the organic-inorganic heterointerfacial interactions, which promote the crystallization of more β-phase [39, 40]. In the XRD pattern, additional characteristic peaks at 2θ = 31.6°, 38.9°, 45.4°and 56.3° correspond to the (110), (111), (200), and (211) crystal planes of the BTO in the P(VDF-TrFE)/BTO-OH/P(VDF-TrFE) sample. These XRD and FTIR results confirm that the BTO-OH nanoparticle layer has been successfully combined with the P(VDF-TrFE) matrix, increasing the β-phase content in the P(VDF-TrFE) material. These findings indicate that, among the three samples, the P(VDF-TrFE)/BTO-OH/P(VDF-TrFE) composite material has the best piezoelectric performance.

3.2 | Performance of SP-Sensor

To investigate the piezoelectric response characteristics of the SP-sensor, as shown in Figure 2a, we have constructed the piezoelectric test system platform, as illustrated in Figure 2b. To evaluate voltage and current outputs, a shaker table was used to apply a stable external force ranging from 5 to 20 N to the SP-sensor at a frequency of 10 Hz. The piezoelectric response voltage and current of the P(VDF-TrFE) sensor are shown in Figure 2c,d, while those of the SP sensor are shown in Figure 2e,f. Under an external force of 20 N, the SP-sensor produced a maximum piezoelectric response voltage of 15 V and a maximum current of 0.97 μA, while the P(VDF-TrFE) sensor generated a maximum voltage of 10.8 V and a current of 0.18 μA. It is evident that adding the BTO-OH nanoparticle layer to the P(VDF-TrFE) results in improved performance, with the open-circuit voltage and current increased by 51.5% and 546%, respectively, compared to the pure P(VDF-TrFE), as shown in Figure 2g. This is due to the introduction of the ceramic piezoelectric material BTO-OH, which has a higher piezoelectric coefficient. The piezoelectric coefficient characterizes the ability of a material to generate an electric field when subjected to an external force.

The relatively high piezoelectric coefficient of the BTO-OH enables the composite material to generate stronger polarization when subjected to the same external force, significantly enhancing the piezoelectric response voltage and current. Meanwhile, the organic-inorganic heterointerfacial interaction between the BTO-OH and P(VDF-TrFE) layers induces an interfacial polarization effect. This effect reduces the activation energy required for the β-phase nucleation and growth via interfacial charge transfer and dipole coupling. The stability of the α-phase is suppressed by space charge fields, while this effect also promotes the transformation of molecular chains into the all-trans β-phase [41]. Consequently, this process enhances the β-phase content in the P(VDF-TrFE) film. The β-phase, a crystalline phase with the highest electric dipole moment, is essential for the piezoelectricity of the P(VDF-TrFE) material. This explains why the composite material with a sandwich structure exhibits superior piezoelectric response performance. Furthermore, we also evaluated the effect of the excitation frequency on the piezoelectric response performance of the sensor. The results of the SP-sensor are shown in Figure 2h,i, while those of the P(VDF-TrFE) sensor are shown in Figure 2j,k. Under a constant external force of 5 N, increasing the excitation frequency does not result in any noticeable change in the piezoelectric voltage or current responses of the P(VDF-TrFE) sensor and the SP-sensor. This indicates that, subjected to the same excitation amplitude, the sensors produce a consistent amount of deformation, which remains unaffected by frequency variations.

To thoroughly investigate the performance of the SP-sensor under various bending states and assess its suitability for bending-related applications in wearable devices, we conducted tests on its piezoelectric response in the bending mode, as shown in Figure 3a,b. Using manual bending with the assistance of a metronome, the P(VDF-TrFE) and SP-sensors were subjected to bending tests at angles of 30°, 45°, 60°, and 90° at a frequency of approximately 4 Hz. As the bending angle increased, the

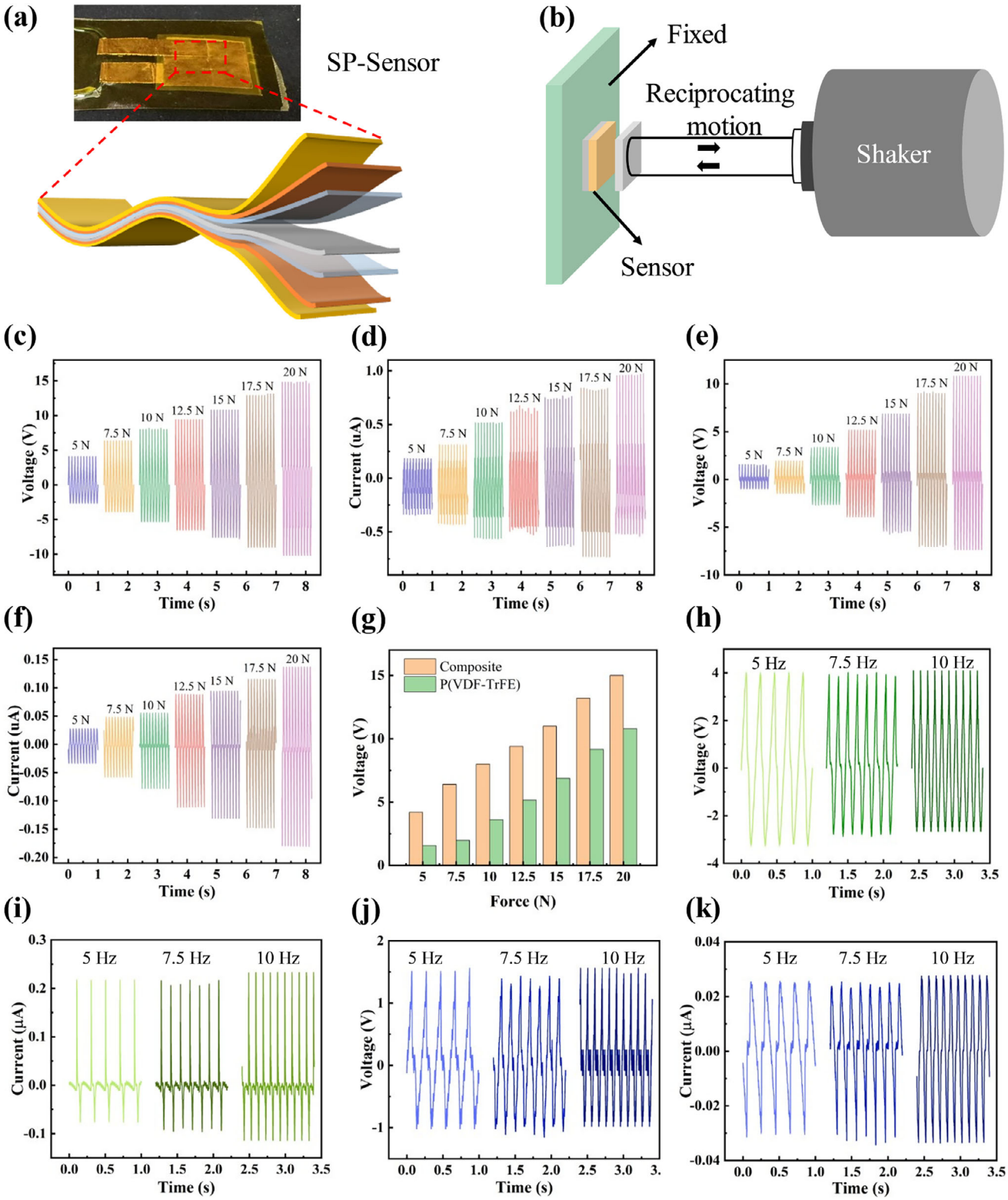

FIGURE 2 | Piezoelectric performance of the SP-sensor. (a) Structure of the SP-sensor. (b) Piezoelectric test platform. (c) Voc and (d) Isc of SP-sensor under different applied forces (5 N–25 N) at 10 Hz. (e) Voc and (f) Isc of the P(VDF-TrFE) sensor under different applied forces (5 N–25 N) at 10 Hz. (g) Comparison of open-circuit voltages between the SP-sensor and P(VDF-TrFE) sensor. (h) Voc and (i) Isc of the SP-sensor under different excitation frequencies. (j) Voc and (k) Isc of the P(VDF-TrFE) sensor under different excitation frequencies.

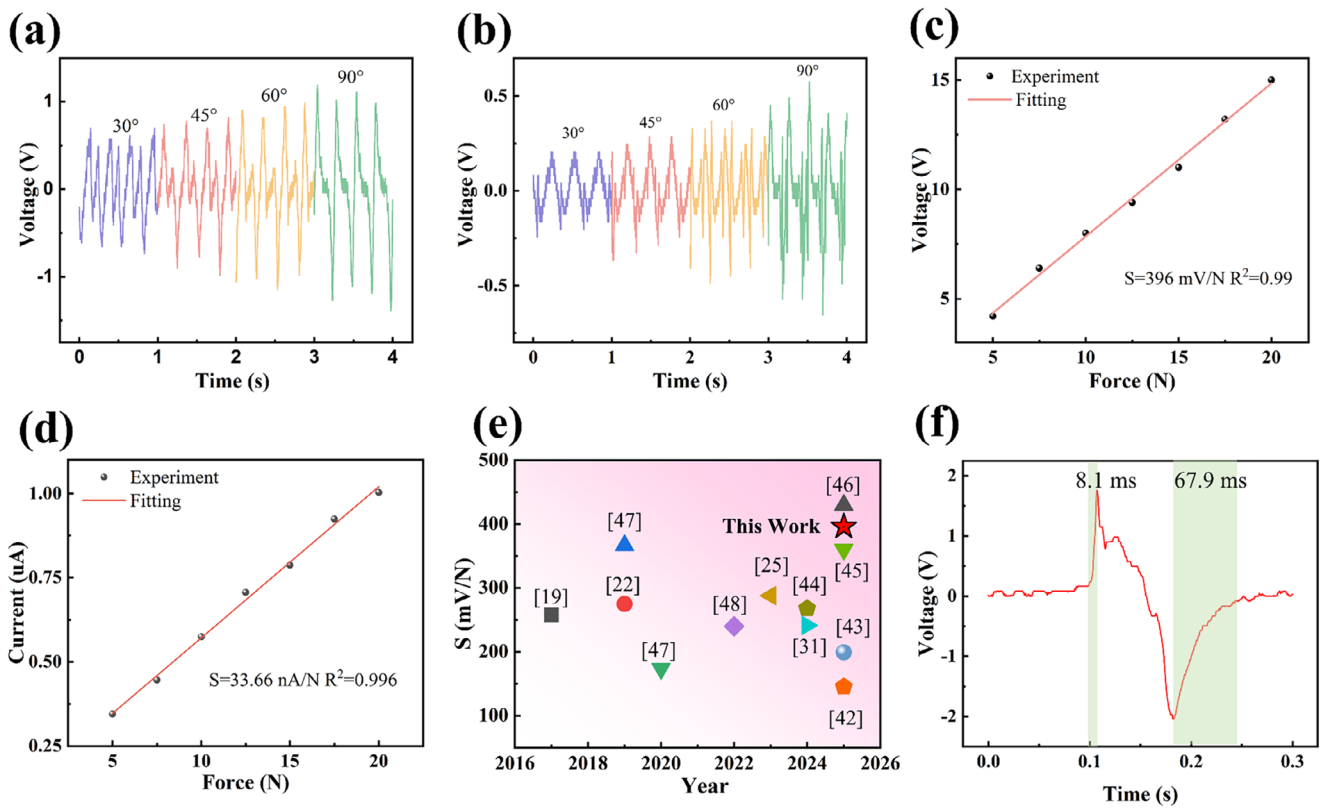

FIGURE 3 | Performance of the sensor. (a) Voc of the SP-sensor under bending at 4 Hz. (b) Voc of the P(VDF-TrFE) sensor under bending at 4 Hz. (c) Voltage sensitivity test curve of the SP-sensor. (d) Current sensitivity test curve of the SP-sensor. (e) Comparison of voltage sensitivity between this work and prior studies. (f) Response time of the SP-sensor.

piezoelectric responses of both sensors increased. When the bending angle reached 90°, the maximum voltage of the SP-sensor was 1.39 V, while the maximum voltage of the P(VDF-TrFE) sensor was 0.573 V. This firmly confirms that after adding the BTO-OH nanoparticle layer to P(VDF-TrFE), its performance is improved, as evidenced by a 142.6% increase in the voltage output compared to pure P(VDF-TrFE).

Sensitivity, response time, and fatigue characteristics are three figures of merit that determine the performance and applicability of sensors. The three indicators not only reflect the accuracy, real-time performance, and reliability of a sensor, but also stand for its practical value in scenarios such as medical care, industry, and consumer electronics. To evaluate the performance of the SP-sensor, we analyzed its force sensitivity, with the results shown in Figure 3c,d. The findings of this study reveal a strong linear relationship between the voltage response from the SP-sensor and the applied force. This relationship can be mathematically described by a function derived using linear fitting. The slope of this line represents the correlation between the voltage output of the SP-sensor and the applied force. It can be seen that its voltage sensitivity is as high as S_v = 396 mV/N with a linearity of R^2 = 0.99, and the current sensitivity is as high as S_A = 33.6 nA/N with a linearity of R^2 = 0.996. As clearly illustrated in Figure 3e, a systematic comparative analysis is conducted between the sandwich-structured composite film developed in this study and similar types of materials in the literature. The results show that, compared with most recently reported piezoelectric films [42–44], our material exhibits superior sensitivity. Its favorable performance is primarily attributed to the incorporation of the BTO-OH nanoparticle interlayer, where the high piezoelectric coefficient of the inorganic ceramic and the enhanced β-phase content of the P(VDF-TrFE) matrix jointly contribute to the overall response. Such a coupled effect leads to a pronounced enhancement in both piezoelectric output and sensitivity of the sandwich-structured composite film. Furthermore, even when benchmarked against a limited number of materials with comparable sensitivity [45, 46], the proposed scheme offers clear advantages in terms of fabrication simplicity and reduced raw material costs. These features render the composite film more compatible with practical applications and large-scale manufacturing. Response time determines perception speed. For example, in electronic skin applications, the sensor's response time is a critical parameter to meet real-time neural feedback requirements. As shown in Figure 3f, the SP-sensor exhibits a response time of 8.1 ms and a recovery time of 67.9 ms.

3.3 | Motion Recognition Application

To evaluate the flexibility of the SP-sensor fabricated from a sandwich-structured composite material, we conducted torsion, folding, and curling tests. It is worth noting that the involved human motion tests were conducted with the informed consent of all volunteers. According to relevant regional regulations, the tests involved non-clinical, non-invasive, and non-toxic wearable sensing, and therefore, formal institutional approval was not required.

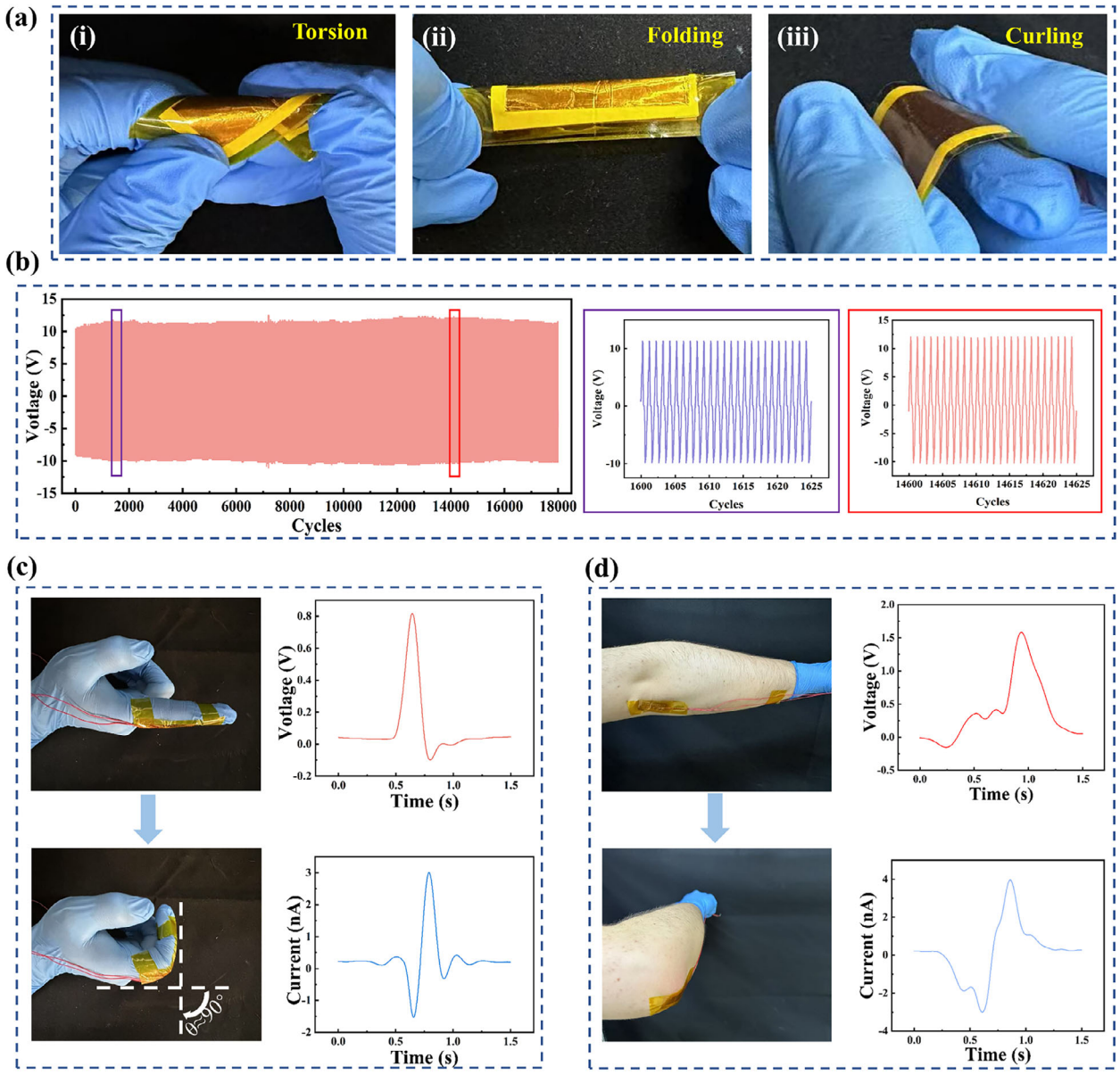

FIGURE 4 | Analysis of human movement signals based on the SP-sensor. (a) Flexibility demonstration of the SP-sensor. (Torsion (i), Folding (ii), and Curling (iii) deformation). (b) Durability test of the SP-sensor. (c) Piezoelectric response during finger bending. (d) Piezoelectric response during elbow bending.

In Figure 4a, the results show that the SP-sensor exhibits exceptional flexibility, allowing for effortless bending and torsion. The stability of a sensor under continuous operation is critical in practical applications. Therefore, to assess the long-term durability of the SP-sensor, a fatigue test was conducted.

During the test, a stable external force of 17.5 N was applied to the SP-sensor for 18,000 cycles, as shown in Figure 4b. The results showed that the voltage of the SP-sensor remained stable at around 12 V throughout the test, demonstrating outstanding stability. Moreover, the randomly selected working segments throughout the entire cycle exhibited highly consistent periodicity. This outcome not only confirms the outstanding mechanical durability and stability of the SP-sensor but also strongly suggests its suitability for continuous long-term operation in daily applications. These excellent properties enable the wearable flexible sensor based on sandwich-structured composite materials to monitor human movements. The SP-sensor was attached to the finger and elbow joints, as shown in Figure 4c,d. When the fingers and elbows were bent to 90° and then restored to their original positions, the SP-sensor generated corresponding piezoelectric outputs. Due to differences in motion amplitude and other characteristics of finger and elbow joints, piezoelectric outputs can serve as a viable option for wearable, flexible sensors. Additionally, it was observed that, regardless of whether the SP-sensor was worn on the finger or the elbow, the current signals displayed more detailed features than the voltage signals. Therefore, the current signal was selected as the primary signal characteristic of the SP-sensor.

When athletes adopt incorrect sports postures, they not only fail to achieve the desired benefits of physical exercise but

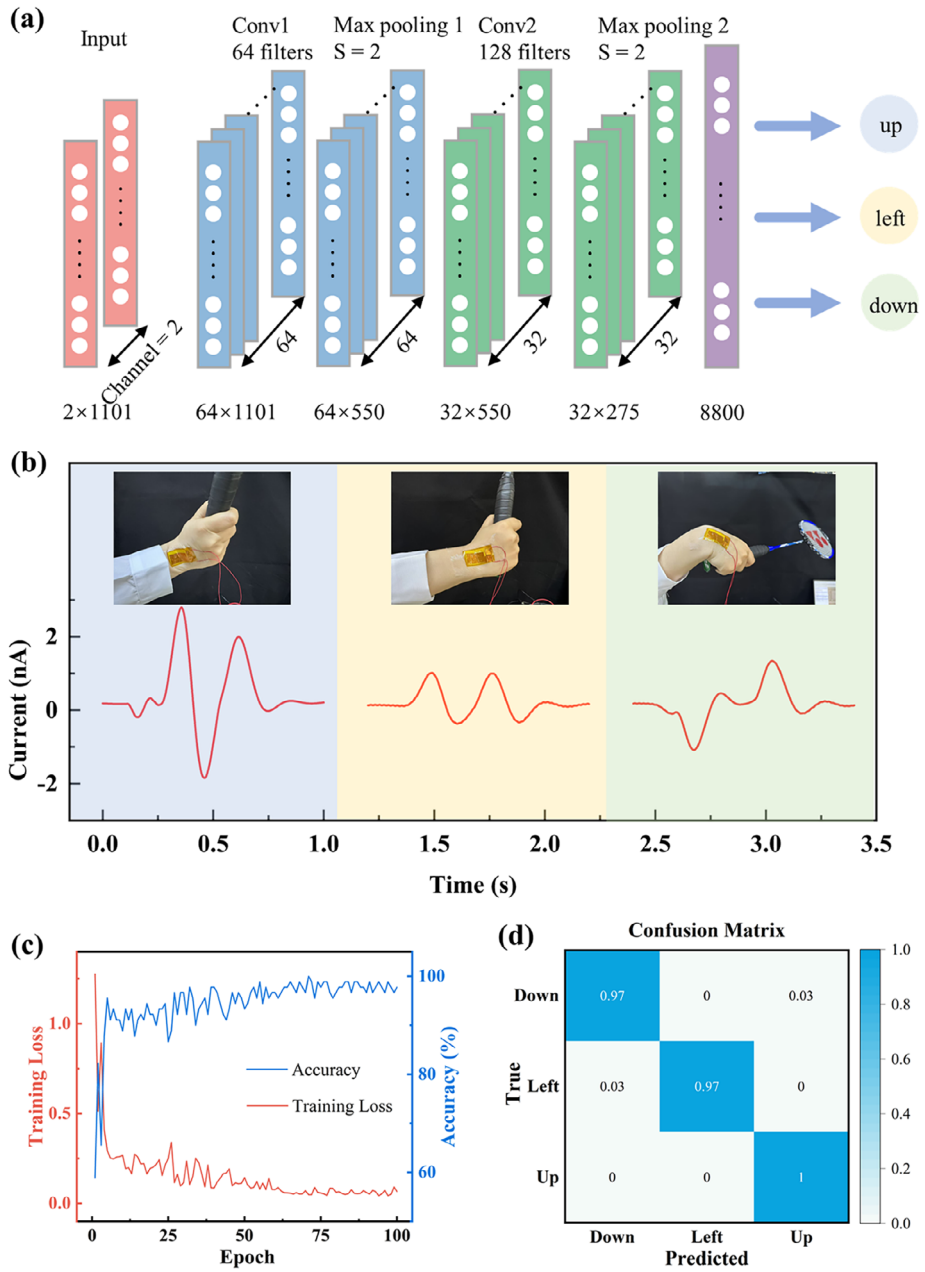

FIGURE 5 | Analysis and recognition of human movements during badminton training based on the signals from the SP-sensor. (a) Structure of the CNN model. (b) Real-time current signals were collected for three wrist movements (up, left, and down). (c) Training accuracy and loss of wrist movements recognition based on the CNN model. (d) Predictive confusion matrix of the CNN model.

also risk harming their bodies. Therefore, accurately identifying movement postures with the aid of sensors and providing real-time feedback is essential. In this study, we attached the SP-sensor to the wrist of a badminton player to precisely capture different current signals generated by various wrist movements. The application tests were intentionally limited to segmented swing motions of badminton players, including upward, downward, and leftward swings, rather than continuous swing actions. This design choice was guided by the specific objective of the work, which is to support basic motion perception and correction for novice badminton players. At the early stage of skill acquisition, novices often struggle to reproduce standard movement patterns, and improper motions can lead to inefficient training or even sports-related injuries. By decomposing complex swing actions into representative elementary motions, the proposed sensor enables clearer signal discrimination and more intuitive feedback for motion learning and correction. Therefore, continuous swing tests were not included at this stage. Wearable sensors are exposed to a variety of interference factors during practical operation, and we have fully considered the potential impacts caused by environmental factors such as skin temperature and sweat. The corresponding mitigation strategies are elaborated as follows:

The core material, P(VDF-TrFE), possesses both piezoelectric and pyroelectric properties; therefore, variations in skin temperature can potentially interfere with the sensor output. However, the pyroelectric effect requires both a temperature difference and a

non-zero temperature change rate. Accordingly, prior to formal testing, the sensor was maintained in close contact with the skin until thermal equilibrium was reached, thereby effectively eliminating interference caused by the pyroelectric effect.

With respect to the influence of perspiration, the sensor design was optimized from two aspects: encapsulation and fixation. Firstly, BTO exhibits extremely high chemical stability, and no toxicity-related reports have been reported in the existing literature. Therefore, it will not irritate human skin under regular contact scenarios. Furthermore, the sealing performance has been enhanced during the sensor packaging process to prevent sweat from contacting the internal sensitive components. Secondly, polyurethane (PU) tape was employed as the adhesive layer. PU tape is widely used in medical applications [47], such as the fixation of indwelling needles, and has excellent biocompatibility and adhesion even under humid conditions. This design not only effectively isolates sweat-related interference but also ensures stable attachment of the sensor during wearing. As a result, the impacts of skin temperature variations and perspiration on signal stability and CNN-based recognition accuracy can be effectively mitigated. These rich and accurate motion-induced sensor data provide a robust and diverse training set for the subsequent deep learning model based on Convolutional Neural Network (CNN). Due to its powerful feature extraction capabilities for handling image and sequence data [30, 48], the CNN model can effectively analyze and classify motion information. The training schematic diagram of the CNN model is shown in Figure 5a. To optimize the CNN model for more accurate recognition, the number of convolutional layers, the number of filters, and the width of the fully connected layers were appropriately adjusted. This model consists of two convolutional layers, with the first layer having 64 filters and the second having 128 filters. A pooling layer with a kernel size and stride of 2×2 is added after each convolutional layer to reduce the spatial dimension [49, 50]. Finally, two fully connected layers are added, with 128 and 256 units, respectively. By using the collected motion information, as shown in Figure 5b, as the input to the CNN-based deep learning model, real-time differentiation among the three wrist movements—wrist depression, wrist dorsiflexion, and wrist movement to the left—is achieved. To guarantee sufficient training data and reliable assessment of model performance, data collected from multiple independent experimental trials were randomly partitioned into training, validation, and test sets at a ratio of 7:1.5:1.5. Such a partitioning strategy, based on repeated experiments, enhances the generalization capability of the model and mitigates potential bias associated with single-session data collection [51]. The training dataset consists of 560 samples, while both the testing dataset and the validation dataset each contain 120 samples. As the number of epochs increases, the training loss of the CNN model steadily decreases, and the training accuracy gradually improves until it finally converges, as shown in Figure 5c.

After nearly 100 epochs, the CNN model achieves a posture recognition accuracy of 100% on the training set. The prediction confusion matrix obtained using the CNN model is shown in Figure 5d, which indicates that the recognition accuracy of the CNN model for these three postures reaches 97.85%. Overall, the CNN recognition model developed in this study effectively aligned with the motion signals captured by the SP-sensor, showcasing the feasibility of the deep learning framework in recognizing and analyzing specific movements in badminton training. This outcome also validates the application of flexible wearable sensors in sports training, providing valuable technical insights and guidance for future research in similar fields.

4 | Conclusion

In this study, a new sandwich-structured composite material, P(VDF-TrFE)/BTO-OH/P(VDF-TrFE), was developed by introducing hydroxyl-modified barium titanate (BTO-OH) nanoparticles into P(VDF-TrFE) matrix through the melt deposition method. This composite material successfully combines the flexibility of P(VDF-TrFE) with the high piezoelectricity of BTO-OH, overcoming the limitations of traditional single-layer piezoelectric sensors. The experimental results show that the SP-sensor fabricated from this novel composite material exhibits a maximum piezoelectric response of 15 V (voltage) and 0.97 μA (current) under an external force of 20 N. These values correspond to a 51.5% increase in voltage and a 546% increase in current relative to the pure P(VDF-TrFE) sensor. The SP-sensor exhibited high sensitivity (396 mV/N for voltage sensitivity and 33.6 nA/N for current sensitivity), excellent durability (no noticeable voltage decay after 18,000 cycles), and fast response and recovery times (8.1 ms for loading and 67.9 ms for recovery). Additionally, the SP-sensor was integrated with a deep learning-based Convolutional Neural Network (CNN) model to achieve real-time identification and classification of human wrist movements, with a recognition accuracy of 97.85%. This work demonstrates the feasibility of using flexible, high-performance piezoelectric sensors for real-time motion monitoring in wearable devices and establishes a foundation for future applications in human-machine interaction, sports training, and medical diagnostics. By integrating AI algorithms with innovative material structures, this study paves the way for the next generation of intelligent wearable sensors. It is worth noting that further optimization of deposition parameters or development of roll-to-roll compatible strategies may be explored in future work, aiming to facilitate large-scale fabrication while enhancing the uniformity of the composite material.

Acknowledgements

This work was supported by the National Natural Science Foundation of China (Grant Nos. 52277227 and 52305135), the Key Scientific and Technological Project of Henan Province (Grant No. 252102241025), the Postdoctoral Research Project of Henan Province (Grant No. 22120024–25), the Guangdong Provincial Project (Grant No. 2023QN10L545), and the Guangzhou Municipal Science and Technology Bureau (Grant Nos. SL2023A03J00869, SL2023A04J01741).

Conflicts of Interest

The authors declare no conflicts of interest.

Data Availability Statement

The data that support the findings of this study are available from the corresponding author upon reasonable request.

References

1. L. Bi, Z. Yang, L. Chen, Z. Wu, and C. Ye, "Compressible Agnws/$Ti_3C_2T_x$ Mxene Aerogel-Based Highly Sensitive Piezoresistive Pressure Sensor as Versatile Electronic Skins," *Journal of Materials Chemistry A* 8 (2020): 20030–20036.

2. T. Huang, S. Yang, P. He, et al., "Phase-Separation-Induced Pvdf/Graphene Coating on Fabrics Toward Flexible Piezoelectric Sensors," *ACS Applied Materials & Interfaces* 10 (2018): 30732–30740.

3. K.-B. Kim, W. Jang, J. Y. Cho, et al., "Transparent and Flexible Piezoelectric Sensor for Detecting Human Movement With a Boron Nitride Nanosheet (Bnns)," *Nano Energy* 54 (2018): 91–98.

4. Z. H. Tang, S. H. Jia, F. Wang, et al., "Highly Stretchable Core–Sheath Fibers via Wet-Spinning for Wearable Strain Sensors," *ACS Applied Materials & Interfaces* 10 (2018): 6624–6635.

5. M. T. Chorsi, E. J. Curry, H. T. Chorsi, et al., "Piezoelectric Biomaterials for Sensors and Actuators," *Advanced Materials* 31 (2019): 1802084.

6. Z. Hanani, I. Izanzar, M. Amjoud, et al., "Lead-Free Nanocomposite Piezoelectric Nanogenerator Film for Biomechanical Energy Harvesting," *Nano Energy* 81 (2021): 105661.

7. H. Xu, W. Zheng, Y. Wang, et al., "Flexible Tensile Strain-Pressure Sensor With an off-Axis Deformation-Insensitivity," *Nano Energy* 99 (2022): 107384.

8. Z. Chai, Y. Sun, Y. He, et al., "Full-Range, High-Sensitivity, Linear Aerogel Pressure Sensor With Epidermal-Inspired Mechanoreception Networks," *Chemical Engineering Journal* 511 (2025): 161886.

9. X. Han, P. Che, L. Jiang, and L. Heng, "Self-Powered Slippery Surface With Photo-Enhanced Triboelectric Signal for Waterproof Wearable Sensor," *Nano Energy* 118 (2023): 109026.

10. G. Tian, W. Deng, Y. Gao, et al., "Rich Lamellar Crystal Baklava-Structured Pzt/Pvdf Piezoelectric Sensor Toward Individual Table Tennis Training," *Nano Energy* 59 (2019): 574–581.

11. W. Deng, T. Yang, L. Jin, et al., "Cowpea-Structured Pvdf/Zno Nanofibers Based Flexible Self-Powered Piezoelectric Bending Motion Sensor towards Remote Control of Gestures," *Nano Energy* 55 (2019): 516–525.

12. M. Bobinger, S. Keddis, S. Hinterleuthner, et al., "Light and Pressure Sensors Based on Pvdf With Sprayed and Transparent Electrodes for Self-Powered Wireless Sensor Nodes," *IEEE Sensors Journal* 19 (2019): 1114–1126.

13. A. Closson, H. Richards, Z. Xu, C. Jin, L. Dong, and J. X. J. Zhang, "Method for Inkjet-Printing Pedot:Pss Polymer Electrode Arrays on Piezoelectric Pvdf-Trfe Fibers," *IEEE Sensors Journal* 21 (2021): 26277–26285.

14. X. Kang, S. Jia, Z. Lin, et al., "Flexible Wearable Hybrid Nanogenerator to Harvest Solar Energy and Human Kinetic Energy," *Nano Energy* 103 (2022): 107808.

15. L. Lu, W. Ding, J. Liu, and B. Yang, "Flexible Pvdf Based Piezoelectric Nanogenerators," *Nano Energy* 78 (2020): 105251.

16. Y. B. Yuan, H. Chen, H. C. Xu, et al., "Highly Sensitive and Wearable Bionic Piezoelectric Sensor for Human Respiratory Monitoring," *Sensors and Actuators A: Physical* 345 (2022): 113818.

17. J. C. Li, J. Yin, M. G. V. Wee, A. Chinnappan, and S. Ramakrishna, "A Self-Powered Piezoelectric Nanofibrous Membrane as Wearable Tactile Sensor for Human Body Motion Monitoring and Recognition," *Advanced Fiber Materials* 5 (2023): 1417–1430.

18. Y. Qi, J. Kim, T. D. Nguyen, B. Lisko, P. K. Purohit, and M. C. McAlpine, "Enhanced Piezoelectricity and Stretchability in Energy Harvesting Devices Fabricated From Buckled Pzt Ribbons," *Nano Letters* 11 (2011): 1331–1336.

19. N. Chamankar, R. Khajavi, A. A. Yousefi, A. Rashidi, and F. Golestanifard, "A Flexible Piezoelectric Pressure Sensor Based on Pvdf Nanocomposite Fibers Doped With Pzt Particles for Energy Harvesting Applications," *Ceramics International* 46 (2020): 19669–19681.

20. X. L. Chen, X. M. Li, J. Y. Shao, et al., "High-Performance Piezoelectric Nanogenerators With Imprinted P(Vdf-Trfe)/Batio Nanocomposite Micropillars for Self-Powered Flexible Sensors," *small* 13 (2017): 1604245.

21. S. Ye, C. Cheng, X. Chen, et al., "High-Performance Piezoelectric Nanogenerator Based on Microstructured P(Vdf-Trfe)/Bnnts Composite for Energy Harvesting and Radiation Protection in Space," *Nano Energy* 60 (2019): 701–714.

22. N. R. Hemanth and B. Kandasubramanian, "Recent Advances in 2d Mxenes for Enhanced Cation Intercalation in Energy Harvesting Applications: A Review," *Chemical Engineering Journal* 392 (2020): 123678.

23. J. E. Ten Elshof, H. Yuan, and P. Gonzalez Rodriguez, "Two-Dimensional Metal Oxide and Metal Hydroxide Nanosheets: Synthesis, Controlled Assembly and Applications in Energy Conversion and Storage," *Advanced Energy Materials* 6 (2016): 1600355.

24. J. Le, F. Lv, J. Lin, et al., "Novel Sandwich-Structured Flexible Composite Films With Enhanced Piezoelectric Performance," *ACS Applied Materials & Interfaces* 16 (2023): 1492–1501.

25. R. Peng, B. Zhang, G. Dong, et al., "Enhanced Piezoelectric Energy Harvester by Employing Freestanding Single-Crystal Batio3 Films in Pvdf-Trfe Based Composites," *Advanced Functional Materials* 34 (2024): 2316519.

26. T. Kim, Y. Shin, K. Kang, et al., "Ultrathin Crystalline-Silicon-Based Strain Gauges With Deep Learning Algorithms for Silent Speech Interfaces," *Nature Communications* 13 (2022): 5815.

27. J. P. Li, Y. Feng, L. Liang, et al., "Flexible Multicavity SERS Substrate Based on Ag Nanoparticle-Decorated Aluminum Hydrous Oxide Nanoflake Array for Highly Sensitive In Situ Detection," *ACS Applied Materials & Interfaces* 16 (2024): 35771–35780.

28. C. Y. Wang, K. L. Xia, H. M. Wang, X. P. Liang, Z. Yin, and Y. Y. Zhang, "Advanced Carbon for Flexible and Wearable Electronics," *Advanced Materials* 31 (2019): 1801072.

29. R. Yamashita, M. Nishio, R. K. G. Do, and K. Togashi, "Convolutional Neural Networks: An Overview and Application in Radiology," *Insights into Imaging* 9 (2018): 611–629.

30. H. Gu, K. Jiang, F. Yu, et al., "Multifunctional Human–Computer Interaction System Based on Deep Learning-Assisted Strain Sensing Array," *ACS Applied Materials & Interfaces* 16 (2024): 54496–54507.

31. Y. Sun, J. Mao, L. Cao, et al., "Intelligent Cardiovascular Disease Diagnosis System Combined Piezoelectric Nanogenerator Based on 2d Bi_2O_2se With Deep Learning Technique," *Nano Energy* 128 (2024): 109878.

32. X. Kang, S. Jia, J. Peng, H. Yu, and X. Zhou, "Electromagnetic-Driven Electrocaloric Cooling Device Based on Ternary Ferroelectric Composites," *Composites, Part B* 227 (2021): 109391.

33. T. Zhou, J.-W. Zha, R.-Y. Cui, B.-H. Fan, J.-K. Yuan, and Z.-M. Dang, "Improving Dielectric Properties of $BaTiO_3$/Ferroelectric Polymer Composites by Employing Surface Hydroxylated $BaTiO_3$ Nanoparticles," *ACS Applied Materials & Interfaces* 3 (2011): 2184–2188.

34. P. Martins, A. C. Lopes, and S. Lanceros-Mendez, "Electroactive Phases of Poly(Vinylidene Fluoride): Determination, Processing and Applications," *Progress in Polymer Science* 39 (2014): 683–706.

35. N. M. Dawson, P. M. Atencio, and K. J. Malloy, "Facile Deposition of High Quality Ferroelectric Poly(Vinylidene Fluoride) Thin Films by Thermally Modulated Spin Coating," *Journal of Polymer Science Part B: Polymer Physics* 55 (2017): 221–227.

36. E. Kabir, M. Khatun, L. Nasrin, M. J. Raihan, and M. Rahman, "Pure B-Phase Formation in Polyvinylidene Fluoride (Pvdf)-Carbon Nanotube Composites," *Journal of Physics D: Applied Physics* 50 (2017): 163002.

37. X. Hu, Y. Jiang, Z. Ma, et al., "Highly Sensitive P(Vdf-Trfe)/Bto Nanofiber-Based Pressure Sensor With Dense Stress Concentration Microstructures," *ACS Applied Polymer Materials* 2 (2020): 4399–4404.

38. J. Gregorio and M. Cestari, "Effect of Crystallization Temperature on the Crystalline Phase Content and Morphology of Poly(Vinylidene Fluoride)," *Journal of Polymer Science Part B: Polymer Physics* 32 (1994): 859–870.

39. Z. Cui, N. T. Hassankiadeh, Y. Zhuang, E. Drioli, and Y. M. Lee, "Crystalline Polymorphism in Poly(Vinylidenefluoride) Membranes," *Progress in Polymer Science* 51 (2015): 94–126.

40. V. Sencadas, S. Lanceros-Méndez, R. Sabater I Serra, et al., "Relaxation Dynamics of Poly (Vinylidene Fluoride) Studied by Dynamical Mechanical Measurements and Dielectric Spectroscopy," *The European Physical Journal E* 35 (2012): 41.

41. M. Samet, V. Levchenko, G. Boiteux, G. Seytre, A. Kallel, and A. Serghei, "Electrode Polarization vs. Maxwell-Wagner-Sillars Interfacial Polarization in Dielectric Spectra of Materials: Characteristic Frequencies and Scaling Laws," *The Journal of Chemical Physics* 142 (2015): 194703.

42. Y. Wu, C.-Y. Tang, S. Wang, et al., "Biomimetic Heteromodulus All-Fluoropolymer Piezoelectric Nanofiber Mats for Highly Sensitive Acoustic Detection," *ACS Applied Materials & Interfaces* 17 (2025): 21808–21818.

43. Y. Zhong, Y. Wang, L. Ma, et al., "Ultrasensitive Piezoelectric Sensor Based on Polyimide Foam for Sound Recognition and Motion Monitoring," *ACS Applied Materials & Interfaces* 17 (2025): 11154–11163.

44. Y. Wang, P. Huang, S. Xu, Y. Luo, and Y. Liu, "Coupling of Fluorescent and Piezoelectric Bifunctions in Pvdf-Hfp Microporous Film With Highly Dispersed Carbon Dots," *Journal of Materials Science: Materials in Electronics* 35 (2024): 1119.

45. Z. Chen, H. Yang, H. Yu, et al., "Comprehensive Effects of Isomeric Doping on Electrospun Pvdf Films: Towards Smart Wiper Systems Enabled by Piezoelectric Nanogenerators and Machine Learning," *Nano Energy* 141 (2025): 111094.

46. Z. Chen, H. Yang, and H. Yu, "PVDF/PANi@ HNT Nanocomposite Membranes: Pioneering Solutions for Piezoelectric Sensing and Energy Harvesting Efficiency," *ACS Applied Materials & Interfaces* 17 (2025): 28668–28681.

47. J. P. Santerre, K. Woodhouse, G. Laroche, and R. S. Labow, "Understanding the Biodegradation of Polyurethanes: From Classical Implants to," *Tissue Engineering Materials* 26 (2005): 7457–7470.

48. D. Guo, Y. Li, Q. Zhou, et al., "Biocompatible, and Flexible Capacitive Pressure Sensor for Intelligent Gait Recognition and Rehabilitation Training," *Nano Energy* 127 (2024): 109750.

49. F. Wen, Z. Zhang, T. He, and C. Lee, "Ai Enabled Sign Language Recognition and Vr Space Bidirectional Communication Using Triboelectric Smart Glove," *Nature Communications* 12 (2021): 5378.

50. R. C. Gonzalez, "Deep Convolutional Neural Networks [Lecture Notes]," *IEEE Signal Processing Magazine* 35 (2018): 79–87.

51. Y. Song, T. Liu, A. Hu, et al., "A Haptic Glove with Flexible Piezoresistive Sensors Made by Graphene and Polyurethane Sponge for Object Recognition Based on Machine Learning Methods," *ACS Applied Electronic Materials* 7 (2025): 3448–3460.